

Early winter barium excess in the Southern Indian Ocean as an annual remineralisation proxy (GEOTRACES GIPr07 cruise)

Natasha René van Horsten^{1,2,3}, H  l  ne Planquette¹, G  raldine Sarthou¹, Thomas James Ryan-Keogh², Nolwenn Lemaitre⁵, Thato Nicholas Mtshali⁴, Alakendra Roychoudhury³, and Eva Bucciarelli¹

¹Univ Brest, CNRS, IRD, Ifremer, LEMAR, F-29280 Plouzane, France.

²SOCCO, CSIR, Lower Hope Road, Cape Town, South Africa, 7700.

³TracEx, Department of Earth Sciences, Stellenbosch University, Stellenbosch, South Africa, 7600.

⁴Department of Forestry, Fisheries and Environment, Oceans and Coast, Foretrust Building, Martin Hammerschlag Way, Cape Town, South Africa, 8001

⁵Department of Earth Sciences, Institute of Geochemistry and Petrology, ETH Zurich, Zurich, Switzerland.

Correspondence to: Natasha van Horsten (nvhorsten@csir.co.za), Eva Bucciarelli (Eva.Bucciarelli@univ-brest.fr)

Abstract. The Southern Ocean (SO) is of global importance to the carbon cycle, and processes such as mesopelagic remineralisation that impact the efficiency of the biological carbon pump in this region need to be better constrained. During this study early austral winter barium excess (Ba_{xs}) concentrations were measured for the first time, along 30  E in the Southern Indian Ocean. Winter Ba_{xs} concentrations of 59 to 684 $\mu\text{mol L}^{-1}$ were comparable to those observed throughout other seasons. The expected decline of the mesopelagic Ba_{xs} signal to background values during winter was not observed, supporting the hypothesis that this remineralisation proxy likely has a longer timescale than previously reported. A compilation of available SO mesopelagic Ba_{xs} data, including data from this study, shows an accumulation rate of $\sim 0.9 \mu\text{mol m}^{-2} \text{d}^{-1}$ from September to July that correlates with temporally integrated remotely sensed primary productivity (PP), throughout the SO from data spanning ~ 20 years, advocating for a possible annual timescale of this proxy. The percentage of mesopelagic POC remineralisation as calculated from estimated POC remineralisation fluxes over integrated remotely sensed PP was ~ 2 fold higher south of the polar front ($19 \pm 15 \%$, $n = 39$) than north of the polar front ($10 \pm 10 \%$, $n = 29$), revealing the higher surface carbon export efficiency further south. By linking integrated remotely sensed PP to mesopelagic Ba_{xs} stock we could obtain better estimates of carbon export and remineralisation signals within the SO on annual and basin scales.

1 Introduction

The Southern Ocean (SO) is a carbon sink of global significance responsible for 40 – 50 % of the global oceans' carbon uptake (Friedlingstein et al., 2019; Gregor et al., 2019; Gruber et al., 2019). Oceanic carbon uptake is regulated by various processes, including the biological carbon pump (BCP). Inorganic carbon is consumed and released by photosynthetic organisms through photosynthesis and respiration (Sarmiento and Gruber, 2006), thereby regulating the earth's carbon cycle by partially

30 sequestering photosynthetically fixed CO₂ in the ocean interior (Honjo et al., 2014). In particular, the SO BCP is a crucial
31 contributor to the earth's carbon cycle by exporting, from surface waters, ~ 3 Pg C yr⁻¹ of the ~ 10 Pg C yr⁻¹ global export
32 production (Schlitzer, 2002). The efficiency of the BCP is linked to the export and preservation of surface particulate matter
33 and is directly linked to atmospheric CO₂ levels, on glacial-interglacial timescales (Honjo et al., 2014; Sigman et al., 2010).
34 Sedimentation out of the surface layer (~100 m) is defined as surface export and out of the mesopelagic zone (~1000 m) as
35 deep export (Passow and Carlow, 2012). There are large gaps in our knowledge with regard to deep carbon export, internal
36 cycling and the seasonality of these processes (Takahashi et al., 2012). The magnitude of deep carbon export is dependent on
37 the efficiency of mesopelagic remineralisation (Jacquet et al., 2015) which can balance or even exceed particulate organic
38 carbon (POC) surface export, especially later in the growing season, thereby limiting deep export (Buesseler and Boyd, 2009;
39 Cardinal et al., 2005; Jacquet et al., 2011, 2015; Lemaitre et al., 2018; Planchon et al., 2013). A possible explanation for
40 imbalances between surface export and mesopelagic processes can be lateral advection of surface waters with lower particle
41 export relative to the mesopelagic signal (Planchon et al., 2013). It is also possible that continued remineralisation of earlier
42 larger export fluxes is detected in the mesopelagic signal but not in the export fluxes of in situ observations (Planchon et al.,
43 2013). In addition to this, the efficiency of remineralisation is influenced by the size and composition of exported particles
44 (Rosengard et al., 2015; Twining et al., 2014) as well as the pathway by which these particles are transported downwards (e.g.,
45 eddy-subduction, active migration, sinking or mixing) from the surface mixed layer to the mesopelagic zone (Boyd et al., 2019;
46 Le Moigne, 2019), creating an intricate web of processes to disentangle. Mesopelagic remineralisation has also been shown to
47 be influenced by environmental factors, such as temperature, phytoplankton community structure and nutrient availability
48 (Bopp et al., 2013; Buesseler and Boyd, 2009). Indeed, nutrient limitation in surface waters limits export and consequently
49 mesopelagic remineralisation by promoting the shift to smaller phytoplankton assemblages that preferentially take up recycled
50 nutrients in the surface mixed layer (Planchon et al., 2013). Phytoplankton community composition exerts an important control
51 where diatoms are more efficiently exported, due to their large size and ballasting by biogenic silica, compared to smaller non-
52 diatom phytoplankton (Armstrong et al., 2009; Buesseler, 1998; Ducklow et al., 2001). Latitudinal trends in remineralisation
53 efficiency can also be linked to temperature-dependent heterotrophs that are responsible for remineralisation (DeVries and
54 Weber, 2017; Marsay et al., 2015). The mesopelagic layer is under-studied, especially in the high latitudes, and therefore these
55 processes are poorly constrained, despite their importance to global elemental cycles, including that of carbon (Le Moigne,
56 2019; Robinson et al., 2010).

57 Export and remineralisation tracers, such as ²³⁴Th/²³⁸U and apparent oxygen utilization (AOU), have been used to study
58 mesopelagic POC remineralisation fluxes (Buesseler et al., 2005; Planchon et al., 2013; Lemaitre et al., 2018). Surface export
59 is set by the deficit of ²³⁴Th activities over ²³⁸U activities, while remineralisation processes are reflected by ²³⁴Th/²³⁸U ratios
60 larger than 1 below the surface mixed layer integrating processes over a 2 to 3 week period (Buesseler et al., 2005; Planchon
61 et al., 2013). AOU is the depletion of oxygen (O₂) in the ocean interior relative to surface saturation, due to biological
62 respiration, when surface water masses are subducted. AOU is dependent on salinity and temperature and integrates
63 remineralisation on timescales of years to decades (Ito et al., 2004). Inaccuracies have, however, been detected with AOU as

64 a remineralisation proxy, specifically in high latitude areas, due to O₂ undersaturation as a consequence of large temperature
65 gradients (Ito et al., 2004).

66 Barium excess (Ba_{xs}) is another proxy utilised to yield estimates of mesopelagic POC remineralisation fluxes. It is defined as
67 the “biogenic” portion of particulate barium (pBa) as barite crystals, formed by the decay of bio-aggregates below the surface
68 mixed layer (Bishop, 1988; Dehairs et al., 1980; Lam and Bishop, 2007; Legeleux and Reyss, 1996; van Beek et al., 2007). As
69 these crystals are released, a Ba_{xs} peak is formed within the mesopelagic zone which has been found to correlate to primary
70 production (PP), O₂ consumption and POC remineralisation (Dehairs and Goeyens, 1996; Dehairs et al., 1997). Depth-
71 integrated rates of O₂ consumption between the base of the mixed layer and 1000 m were estimated using an inverse 1-D
72 advection-diffusion-consumption model (Shopova et al., 1995) to develop transfer functions between the Ba_{xs} signal and the
73 rate of surface POC export for subsequent mesopelagic remineralisation (Dehairs and Goeyens, 1996; Dehairs et al., 1997).
74 Strong correlations have been obtained between the well-established export/remineralisation flux proxy ²³⁴Th and Ba_{xs}, during
75 studies conducted in the SO and the North Atlantic, confirming the validity of Ba_{xs} as a remineralisation proxy (Cardinal et
76 al., 2005; Lemaitre et al., 2018; Planchon et al., 2013). Estimates of POC remineralisation fluxes, using the Ba_{xs} proxy, are
77 directly influenced by the background signal of Ba_{xs}, after partial dissolution and sedimentation from the previous bloom
78 season. It can be thought of as “pre-formed Ba_{xs}”, defined as the Ba_{residual} signal at zero O₂ consumption (Jacquet et al., 2015).
79 Because studies conducted in spring and summer suggest that the mesopelagic Ba_{xs} signal lasts between a few days to a few
80 weeks (Dehairs et al., 1997; Cardinal et al., 2005; Jacquet et al., 2007, 2008a), it is postulated that winter measurements should
81 give the true SO Ba_{residual} value (Jacquet et al., 2008b, 2011). In this context, as part of a GEOTRACES process study (GIpr07)
82 of a transect along 30°E in the Southern Indian Ocean (58.5°S to 41.0°S), we studied Ba_{xs} distributions during early austral
83 winter (July 2017) to better constrain the SO Ba_{residual} concentrations and the timescale of this proxy. To our knowledge these
84 are the first reported wintertime values for this proxy in the SO.

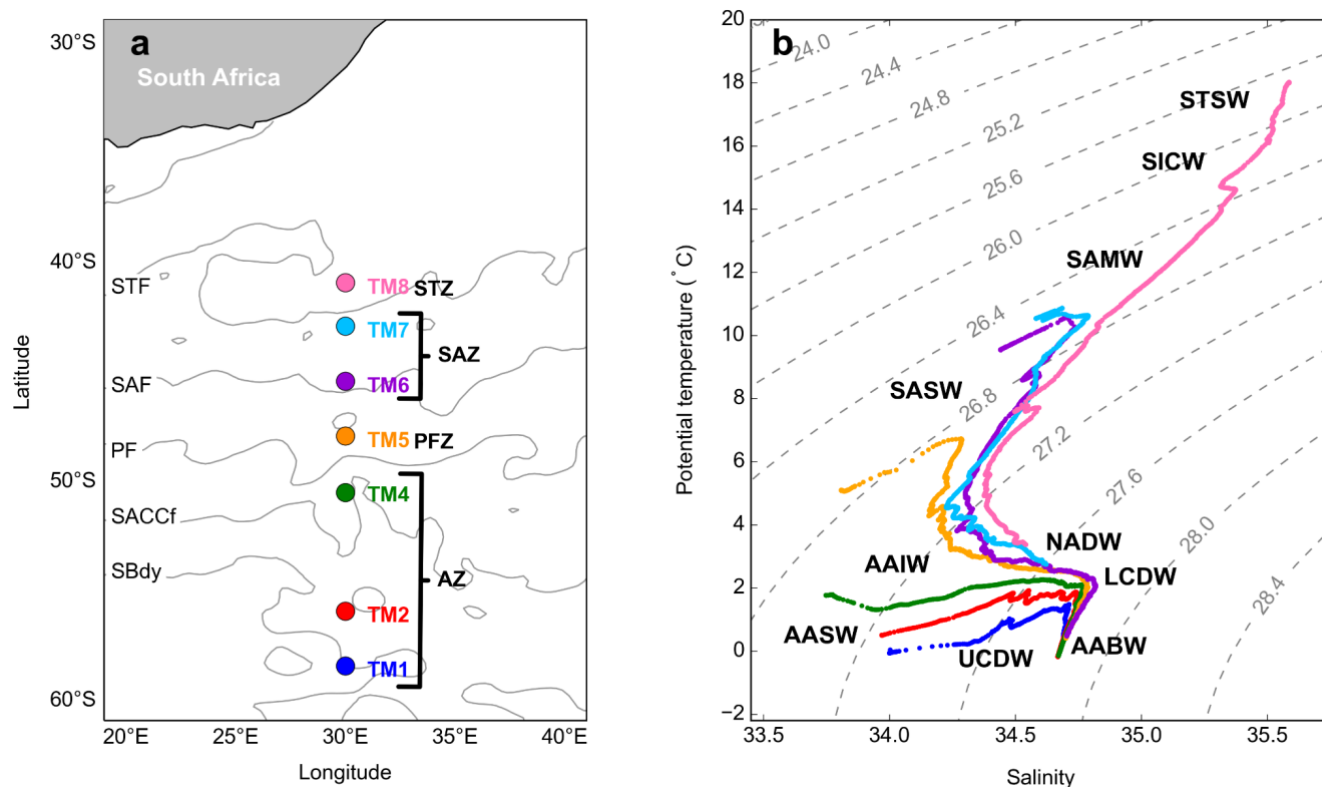
85 **2 Materials and Methods**

86 **2.1 Sampling and hydrography**

87 During the GEOTRACES GIpr07 cruise, which took place in early austral winter (28 June - 13 July 2017) onboard the R/V
88 *SA Agulhas II*, seven stations were sampled along 30°E, from 58.5°S to 41.0°S (WOCE I06S, Figure 1a). At each station
89 between 15 and 21 samples were collected from 25 m down to 1500 m, for shallow stations, and down to 4250 m, for deep
90 stations, to be analysed for multiple parameters.

91 Positions of the fronts during the cruise were determined using the July monthly mean absolute dynamic topography data from
92 the CLS/AVISO product (Rio et al., 2011), with boundary definitions from Swart et al. (2010). From north to south the
93 identified fronts are, the Subtropical Front (STF), the Subantarctic Front (SAF), the Polar Front (PF), the Southern Antarctic
94 Circumpolar Current Front (SACCf) and the Southern Boundary (SBdy) (Figure 1a). The marginal ice zone, identified as the

95 position of 30 % ice cover, was positioned at 61.7°S, approximately 3° (356 km) south of the southernmost station (de Jong et
 96 al., 2018). Therefore, a potential sea ice influence on our study area can be disregarded.



97
 98 **Figure 1:** (a) GEOTRACES GIPr07 cruise sampling stations overlaid on a map with frontal positions; namely, the Subtropical Front
 99 (STF), the Subantarctic Front (SAF), the Polar Front (PF), the Southern Antarctic Circumpolar Current Front (SACCf) and the
 100 Southern Boundary (SBdy), as determined by mean absolute dynamic topography (MADT) and crossing over four zones; namely,
 101 the Antarctic zone (AZ), the Polar frontal zone (PFZ), the Subantarctic zone (SAZ) and the Subtropical zone (STZ). (b) Potential
 102 temperature plotted against salinity, overlaid on isopycnals and identification of water masses sampled; namely, Subtropical Surface
 103 Water (STSW), South Indian Central Water (SICW), Subantarctic Mode Water (SAMW), Subantarctic Surface Water (SASW),
 104 Antarctic Intermediate Water (AAIW), Antarctic Surface Water (AASW), North Atlantic Deep Water (NADW), Lower
 105 Circumpolar Deep Water (LCDW), Upper Circumpolar Deep Water (UCDW), and Antarctic Bottom Water (AABW).

106 2.2 Temperature, salinity and dissolved O₂

107 Temperature (°C), salinity and dissolved O₂ (μmol L⁻¹) profiles were measured by sensors (SBE 911plus) which were
 108 calibrated by the manufacturer within a year prior to the cruise. At each cast, discrete seawater samples were collected and
 109 analysed onboard for in situ calibration of sensor data for salinity (8410A Portasal salinometer, R² = 0.99) and dissolved O₂
 110 concentrations (Metrohm 848 titrino plus, R² = 0.83; Ehrhardt et al., 1983). Temperature and salinity measurements were used
 111 to calculate potential density (σ_θ; Gill, 1982) to characterise water masses sampled and to identify the mixed layer depth
 112 (MLD). The MLD is the depth at which there is a change of 0.03 kg m⁻³ in σ_θ from a near-surface value at ~ 10 m (de Boyer
 113 Montégut, et al., 2004). Decreases in dissolved O₂ concentrations at intermediate depths, together with Ba_{xs} concentrations,
 114 were used to define the mesopelagic remineralisation layer.

115 **2.3 pBa and pAl**

116 Profile sampling of the water column was conducted with a GEOTRACES compliant trace metal clean CTD housed on an
 117 epoxy coated aluminium frame with titanium bolts equipped with 24 x 12 L trace metal clean Teflon coated GO-FLO bottles
 118 (General Oceanics). All sampling and analyses were conducted following the GEOTRACES clean sampling and analysis
 119 protocols (Cutter et al., 2017). Volumes of 2 to 7 L seawater were filtered from the GO-FLO bottles onto acid-washed
 120 polyethersulfone filters (25 mm diameter, Supor, 0.45 µm pore size), for pBa and pAl analyses. Filters were mounted in-line
 121 on the side spigot of each Go-Flo bottle, on swinnex filter holders. Furthermore, bottles were mixed 3 times before filtration,
 122 as recommended by the GEOTRACES protocols (Cutter et al., 2017), to ensure homogenous sampling. Although the large
 123 fast-sinking fraction of particles may be undersampled by using bottles (Bishop and Edmond, 1976; Planquette and Sherrell,
 124 2012), comparing data that were generated using the same, internationally validated sampling systems and protocols (Cutter
 125 et al. 2017), as we do in this study, minimises potential bias. After filtration, filters were placed in trace metal clean petri slides
 126 (Pall) and kept frozen at -20°C until further processing on land. Sample processing was conducted under a class 100 HEPA
 127 filtered laminar flow and extraction hood in a clean laboratory.

128 The pBa and pAl samples were processed and analysed 6 months after sample collection, at LEMAR (France). Unused blank
 129 filters and filters containing the samples were acid reflux digested at 130°C in acid-cleaned savillex vials using a mixture of
 130 HF and HNO₃ (both Ultrapure grade, Merck) solutions (Planquette and Sherrell, 2012). Archive solutions were stored in 3 ml
 131 of 0.12 M HNO₃ (Ultrapur grade), of which 250 µL was diluted up to 2 mL for analysis by sector field inductively coupled
 132 plasma mass spectrometry (SF-ICP-MS, Element XR Thermo Scientific). Samples were spiked with 1 µg L⁻¹ indium as an
 133 internal standard to correct for instrument drift. The detection limits, defined as three times the standard deviation of the blanks
 134 (unused filter blanks), were 0.39 pmol L⁻¹ and 0.03 nmol L⁻¹ (n = 5) for pBa and pAl, respectively. Mean amounts (in nmol)
 135 of a given element determined in unused filter blanks were subtracted from the amounts in the sample filter then divided by
 136 the volume filtered. Three certified reference materials (BCR 414, MESS 4 and PACS 3) were processed and analysed with
 137 the samples to assess the accuracy of the methodology. Our values were in good agreement with the certified values of the
 138 reference materials (Table 1) (Jochum et al., 2005). Percentage error of analyses was determined by the repeat analysis of
 139 random samples during each run, the mean percentage error of sample analysis for pBa and pAl was 9.2 ± 2.5 % and 11.1 ±
 140 4.6 % (mean ± SD, n = 6), respectively.

141 **Table 1: Certified Reference Material recovery data for accuracy determination of pBa and pAl analyses**
 142 **N/A refers to instances where there are no certified values available to check for accuracy**

	pBa (mg/kg)	pAl (mg/kg)
PACS 3 certified (mean ± SD)	N/A	65800 ± 1700
PACS 3 measured (mean ± SD)	N/A	73156 ± 15416
PACS 3 mean % recovery	N/A	111 ± 23

MESS 4 certified	920	79000 ± 2000
MESS 4 (mean ± SD)	1033 ± 28	100048 ± 26870
MESS 4 mean % recovery ± SD	112 ± 3	127 ± 34
BCR 414 indicative values	32 ± 5	2384 ± 652
BCR 414 (mean ± SD)	34 ± 4	2651 ± 317
BCR 414 mean % recovery ± SD	105 ± 12	111 ± 13

143

144 **2.4 Ba_{xs} as a proxy for mesopelagic POC remineralisation**

145 The non-lithogenic fraction of pBa, Ba_{xs}, was calculated by subtracting the lithogenic fraction of pBa from the total pBa
146 measured using Eq. 1. The lithogenic contribution to pBa was calculated by multiplying the pAl concentration with the Ba/Al
147 upper continental crust (UCC) ratio, 0.00135, as determined by Taylor and McLennan (1985).

148

$$149 \text{Ba}_{xs} = [\text{pBa}] - ([\text{pAl}] \times (\text{Ba}/\text{Al})_{\text{UCC}}) \quad (1)$$

150

151 Total pBa and Ba_{xs} profiles were nearly identical with a mean percentage Ba_{xs} to total pBa of 99 ± 1 % (mean ± SD, n = 124;
152 Table S2), indicating that pBa from lithogenic sources was negligible. This ensures the accurate estimation of Ba_{xs}, which
153 requires that less than 50 % of pBa should be associated with lithogenic inputs (Dymond et al., 1992).

154 The mesopelagic POC remineralisation flux was estimated using Eq. 2 (Dehairs and Goeyens, 1996; Shopova et al., 1995):

155

$$156 \text{Mesopelagic POC remineralisation} = Z \times \text{JO}_2 \times (\text{C}:\text{O}_2)_{\text{Redfield Ratio}} \times 12.01 \quad (2)$$

157

158 Where the mesopelagic POC remineralisation flux is expressed in mg C m⁻² d⁻¹, Z is the depth range of the mesopelagic Ba_{xs}
159 layer (100 - 1000 m), C:O₂ is the stoichiometric molar ratio of carbon to O₂ consumption by remineralisation as per the Redfield
160 Ratio (127/175, Broecker et al., 1985), 12.01 is the molar mass of carbon (g mol⁻¹) and JO₂ is the rate of O₂ consumption (μmol
161 L⁻¹ d⁻¹) as estimated using Eq. 3:

162

$$163 \text{JO}_2 = (\text{Mesopelagic Ba}_{xs} - \text{Ba}_{\text{residual}})/17200 \quad (3)$$

164

165 Eq. 3 (Dehairs and Goeyens, 1996; Shopova et al., 1995) is the linearisation of the exponential function by Dehairs et al.
166 (1997). Mesopelagic Ba_{xs} is the depth-weighted average Ba_{xs} of the mesopelagic zone (pmol L⁻¹), the constant value of 17200
167 is the slope of the linear regression of depth-weighted average Ba_{xs} (pmol L⁻¹) versus O₂ consumption rate (μmol L⁻¹ d⁻¹) and

168 Ba_{residual} is the deep ocean background value of Ba_{xs} at zero oxygen consumption. The literature value of $180 \mu\text{mol L}^{-1}$ was
169 used as the Ba_{residual} value (Jacquet et al, 2008a; 2008b; 2011; 2015; Planchon et al., 2013) in our calculations.
170 The integrated mesopelagic Ba_{xs} stock ($\mu\text{mol m}^{-2}$) over the mesopelagic layer (100 - 1000 m) was calculated from the depth-
171 weighted average Ba_{xs} in order to investigate the link between the accumulated mesopelagic signal and the corresponding
172 integrated remotely sensed primary productivity (PP).

173 **2.5 Integrated remotely sensed PP**

174 The integrated remotely sensed PP ($\text{mg C m}^{-2} \text{d}^{-1}$) within the surface mixed layer was calculated using the CbPM algorithm
175 (Behrenfeld et al., 2005), which requires chlorophyll concentration (mg m^{-3}), particulate backscatter ($\lambda 443 \text{ nm}$, m^{-1}),
176 photosynthetically active radiation (PAR; $\mu\text{mol photons m}^{-2} \text{d}^{-1}$) and the MLD (m). Ocean Colour-Climate Change Initiative
177 (OC-CCI) data (<https://esa-oceancolour-cci.org/>), which blends existing data streams into a coherent record, meeting the
178 quality requirements for climate assessment (Sathyendranath et al., 2019), were used for chlorophyll and particulate
179 backscatter. PAR was taken from GLOB colour (<http://www.globcolour.info/>), and the MLD was taken from the climatology
180 of de Boyer Montegut et al. (2004). The integrated remotely sensed PP data were regridded to 0.25° spatially, using bilinear
181 interpolation using the Python programming package xESMF (Zhuang, 2018), and averaged monthly. The area-averaged PP
182 was averaged over a $6 \times 1^\circ$ rectangular sample area, positioned 6° upstream longitudinally, and 1° latitudinally centred around
183 each sampled station (see discussion for details). In order to assess the validity of the remotely sensed PP data and demonstrate
184 no meridional bias across the SO, the percentage valid pixels was calculated for data north ($90 \pm 20 \%$; mean \pm SD, $n = 370$)
185 and south ($82 \pm 29 \%$ mean \pm SD, $n = 488$) of the PF, revealing no bias.

186 **2.6 Integrated % POC remineralised**

187 The integrated remineralised POC (mg C m^{-2}) was estimated by multiplying the POC remineralisation flux ($\text{mg C m}^{-2} \text{d}^{-1}$), as
188 estimated using the Ba_{xs} proxy method, by the number of days over which the corresponding remotely sensed PP ($\text{mg C m}^{-2} \text{d}^{-1}$)
189 was subsampled. The % POC remineralised was then estimated as the percentage of integrated remotely sensed PP (mg C
190 m^{-2}) remineralised, assuming that the mesopelagic Ba_{xs} stock signal observed is due to the remineralisation of the integrated
191 surface PP signal.

192 **2.7 Statistical analysis**

193 For statistical analysis, the least squares regression method was applied for assessment of significant correlations (Barbur et
194 al., 1994). Significant differences between regions and regressions were tested using Welch's t-test, with an alpha of 0.05 (95
195 % confidence level) (Kokoska and Zwillinger, 2000).

196 3 Results

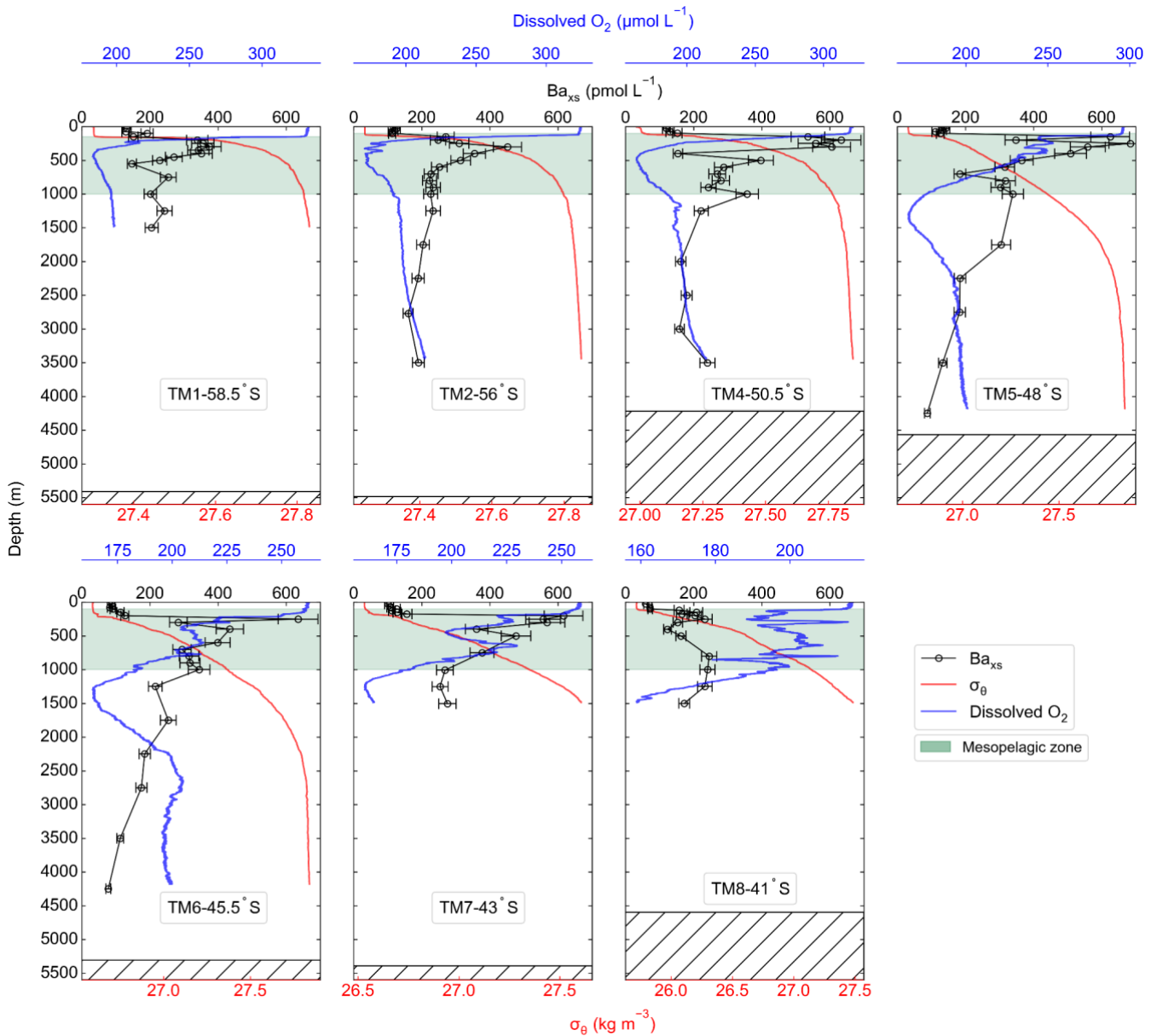
197 3.1 Hydrography

198 The potential temperature (θ) and salinity (S) along the transect ranged from -0.06 to 18.03 °C and from 33.77 to 35.59,
199 respectively. Where surface θ and S define four hydrographic zones; namely, the Antarctic zone (AZ; $\theta < 2.5$ °C; $S \leq 34$) from
200 $\sim 50^\circ\text{S}$ to 58.5°S , the polar frontal zone (PFZ; $\theta \cong 5$ °C; $S \cong 33.8$) at $\sim 48^\circ\text{S}$, the subantarctic zone (SAZ; $5 < \theta < 11$ °C; 33.8
201 $< S < 34.7$) between 43°S and 45.5°S , and the subtropical zone (STZ; $\theta \geq 17.9$ °C; $S \cong 35.6$) at 41°S (Figure 1a; Anilkumar
202 and Sabu, 2017; Orsi et al., 1995; Pollard et al., 2002). The MLDs along the transect ranged between 97 and 215 m (144 ± 39
203 m; mean \pm SD, $n = 7$), shoaling towards the PF (Table S1).

204 As can be observed on the T-S plot of stations sampled (Figure 1b), different water masses were sampled along the transect
205 throughout the water column. South of the polar front (SPF; $\cong 50^\circ\text{S}$; TM1, 2 and 4), from surface to depth, Antarctic Surface
206 Water (AASW; $27 < \sigma_\theta < 27.4$ kg.m⁻³), Upper and Lower Circumpolar Deep Water (UCDW; $27.2 < \sigma_\theta < 27.75$ kg.m⁻³ and
207 LCDW; $27.75 < \sigma_\theta < 27.85$ kg.m⁻³, respectively), and Antarctic Bottom Water (AABW; $27.8 < \sigma_\theta < 27.85$ kg.m⁻³) were
208 characterised. North of the polar front (NPF) and south of the STF ($< 50^\circ\text{S}$; TM5, 6 and 7), from surface to depth, Subantarctic
209 Surface Water (SASW; $26.5 < \sigma_\theta < 26.75$ kg.m⁻³), Antarctic Intermediate Water (AAIW; $26.7 < \sigma_\theta < 27.4$ kg.m⁻³), North
210 Atlantic Deep Water (NADW; $27 < \sigma_\theta < 27.85$ kg.m⁻³) and, as far north as 45.5°S , AABW close to the ocean floor, were
211 identified. At the northernmost station (TM8; 41°S), in the STZ, the water masses sampled include Subtropical Surface Water
212 (STSW; $\sigma_\theta \cong 25.7$ kg.m⁻³), South Indian Central Water (SICW; $25.8 < \sigma_\theta < 26.2$ kg.m⁻³), Subantarctic Mode Water (SAMW;
213 $26.2 < \sigma_\theta < 26.6$ kg.m⁻³), AAIW and NADW.

214 3.2 Dissolved O₂

215 The water column dissolved O₂ concentrations ranged from 159 to 333 $\mu\text{mol L}^{-1}$ (Figure 2). Maximum concentrations were
216 observed in the surface mixed layer, increasing southwards along the transect, with a mean value of 287 ± 40 $\mu\text{mol L}^{-1}$ (mean
217 \pm SD, $n = 700$). A decrease in concentrations below the MLD coincided with an increase in σ_θ . South of the PF, the decrease
218 in dissolved O₂ concentrations at the MLD was sharp and relatively shallow when compared to profiles NPF, which were more
219 gradual, spanning a wider depth range. Within the mesopelagic zone concentrations decreased down to 204 ± 29 $\mu\text{mol L}^{-1}$
220 (mean \pm SD, $n = 6373$), then remained relatively uniform below 1000 m at 192 ± 113 $\mu\text{mol L}^{-1}$ (mean \pm SD, $n = 12950$).



221
222
223
224

Figure 2: Ba_{xs} (black circles) with error bars, potential density (σ_θ ; red) and dissolved O_2 (blue) profiles sampled along the transect, plotted against depth, for stations TM1 to TM8, from south to north. The green shaded area is the mesopelagic zone, and the hatched area is the ocean floor.

225 3.3 Ba_{xs} and estimated POC remineralisation fluxes

226 Along the transect, Ba_{xs} concentrations ranged from 59 to 684 pmol L^{-1} . All profiles exhibited a depletion of Ba_{xs} in the upper
227 surface waters (59 - 152 pmol L^{-1}), then a rapid increase below the MLD (~ 150 m), with concentrations ranging between 113
228 and 684 pmol L^{-1} in the mesopelagic zone (100 - 1000 m, Figure 2). At the two southernmost stations (TM1 and TM2),

229 mesopelagic Ba_{xs} peaks spanned a narrower depth range (100 - 600 m) than stations further north, with concentrations reaching
230 values of $\sim 400 \text{ pmol L}^{-1}$. Concentrations were higher in the PFZ and SAZ with a maximum of 684 pmol L^{-1} in the PFZ, at
231 48°S (TM5). The subsurface increase of Ba_{xs} started at slightly deeper depths (150 - 200 m) and spanned wider depth ranges
232 down to 1000 m, at stations north of the PF. The STZ station, at 41°S (TM8), had the lowest concentrations, only increasing
233 up to $\sim 200 \text{ pmol L}^{-1}$. Double peaks were observed at all stations north of the PF, with a shallow and more substantial peak
234 occurring in the upper mesopelagic zone and a second peak in the lower mesopelagic zone. Below the mesopelagic zone, Ba_{xs}
235 concentrations decreased down to $\sim 180 \text{ pmol L}^{-1}$ and remained relatively uniform.

236 The mean Ba_{residual} concentration south of PF was $183 \pm 29 \text{ pmol L}^{-1}$ (mean \pm SD, $n = 7$), whereas it was $142 \pm 45 \text{ pmol L}^{-1}$
237 (mean \pm SD, $n = 8$) between the PF and the STF. The two regions were however not significantly different to each other when
238 conducting a Welch's t-test (t-statistic = 2.10; p-value = 0.06) and when averaging all concentrations below 2000 m along the
239 transect, the Ba_{residual} concentration was $161 \pm 43 \text{ pmol L}^{-1}$ (mean \pm SD, $n = 15$). This concentration is not statistically different
240 from the literature value of 180 pmol L^{-1} (Jacquet et al, 2008a; 2008b; 2011; 2015; Planchon et al., 2013), which is widely
241 used for estimates of POC remineralisation fluxes. For a better comparison with these previous estimates, we used 180 pmol
242 L^{-1} for the Ba_{residual} concentration in our calculations.

243 The estimated POC remineralisation fluxes for the study area ranged from 6 to $96 \text{ mg C m}^{-2} \text{ d}^{-1}$ (Table S3), increasing
244 northwards from the southernmost station up to the PFZ from 32 to $92 \text{ mg C m}^{-2} \text{ d}^{-1}$, then decreasing down to $70 \text{ mg C m}^{-2} \text{ d}^{-1}$
245 at the SAF. The highest flux was estimated in the SAZ, and the lowest flux was estimated in the STZ.

246 4 Discussion

247 4.1 Early wintertime Ba_{xs} and Ba_{residual} concentrations

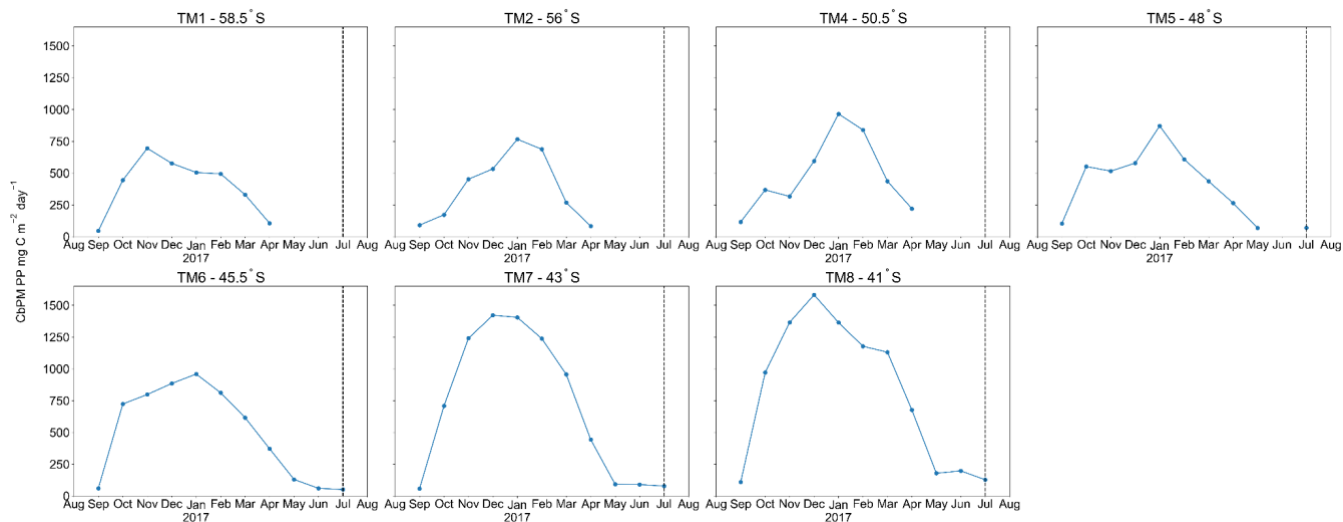
248 A noticeable difference between profiles sampled early in the bloom season (Dehairs et al., 1997; Jacquet et al., 2015) versus
249 those sampled later (Cardinal et al., 2001; Planchon et al., 2013) is the contrasted Ba_{xs} concentrations in the surface mixed
250 layer. Dehairs et al. (1997) has shown that these concentrations of Ba_{xs} can be as high as 9000 pmol L^{-1} in areas of high
251 productivity during spring, which then become depleted to concentrations below the SO Ba_{residual} value of $\sim 180 \text{ pmol L}^{-1}$, as
252 productivity declines and surface POC export increases (Planchon et al., 2013). These high surface concentrations are,
253 however, not due to the same process as the one that controls the Ba_{xs} concentrations within the mesopelagic zone (Jacquet et
254 al., 2011). Surface water concentrations are associated with Ba adsorbed onto particles whereas the mesopelagic Ba_{xs} signal is
255 due to barite crystals formed within decaying bio-aggregates (Cardinal et al., 2005; Lam and Bishop, 2007; Lemaitre et al.,
256 2018; Sternberg et al., 2005). In this study, we observed surface depletion of Ba_{xs} at all stations, in line with the assumption
257 that the bulk surface export from the preceding bloom had been achieved at the time of sampling and, the majority of the Ba_{xs}
258 had been transferred to the mesopelagic zone.

259 A sharp increase in σ_θ observed at the MLD has previously been identified as the depth at which decaying bio-aggregates are
260 formed (Lam and Bishop, 2007). These increases coincided with an increase in Ba_{xs} (Figure 2), linking the subsurface Ba_{xs}

261 signal to decaying bio-aggregates as per previous studies (Cardinal et al., 2005; Dehairs et al., 1997; Jacquet et al., 2011).
262 Additionally, decreases observed in dissolved O₂ profiles along the transect were also accompanied by coinciding increases in
263 Ba_{xs}, in line with O₂ consumption due to remineralisation within the mesopelagic zone (Figure 2) (Cardinal et al., 2005; Jacquet
264 et al., 2005, 2011). The observed range of mesopelagic Ba_{xs} concentrations (113 - 684 pmol L⁻¹) were comparable to those
265 previously reported in SO open waters (~ 200 - 1000 pmol L⁻¹; Cardinal et al., 2001, 2005; Jacquet et al., 2005, 2008a, 2008b,
266 2011, 2015; Planchon et al., 2013).

267 Ba_{xs} profiles exhibited similar distributions to those reported throughout bloom seasons in the SO, with distinct peaks observed
268 within the mesopelagic zone at all stations. Earlier in the bloom season, peaks mostly occur within the upper half of the
269 mesopelagic zone (100 - 500 m: Cardinal et al., 2001, 2005; Jacquet et al., 2005, 2008a, 2011, 2015), but as the season
270 progresses, they deepen down towards the bottom half of the mesopelagic zone (500 - >1000 m: Jacquet et al., 2008b, Planchon
271 et al., 2013). Deepening and widening of the remineralisation depth range can be expected as the season progresses, due to
272 continued remineralisation taking place as particles sink to the bottom of the mesopelagic zone (Lemaitre et al., 2018; Planchon
273 et al., 2013). This is also what we observed during early winter at stations NPF, with a second peak in deeper waters, as
274 observed by Jacquet et al. (2008b) during the iron (Fe) fertilisation experiment (EIFEX). The deeper peak could also be linked
275 to relatively larger cells that sink faster as they remineralise, possibly a large bloom earlier in the season.

276 A distinct latitudinal trend in mesopelagic depth-weighted average Ba_{xs} has generally been observed in the SO with the highest
277 values in the PFZ, decreasing north and southwards from the PF. These latitudinal trends tend to be accompanied by a
278 coinciding trend in in situ surface biomass measurements (Cardinal et al., 2005; Dehairs et al., 1997, Jacquet et al., 2011;
279 Planchon et al., 2013). During our early winter study, we observed a similar latitudinal trend in mesopelagic Ba_{xs} stock (μmol
280 m⁻²), with an increase from the southernmost station up to the PF, then varying around a maximum in the SAZ, down to the
281 lowest value in the STZ, whereas temporally integrated remotely sensed PP increased progressively northwards to a maximum
282 in the STZ (Figure S1). Time of sampling and extended blooms, which are characteristic of the SAZ (Thomalla et al., 2011),
283 could be contributing factors to the higher values observed in PP and mesopelagic Ba_{xs} distributions at stations north of the PF
284 (Figure S1). Contrary to what was expected, the profiles observed during our early winter study still show a significant
285 mesopelagic remineralisation signal, well after the summer bloom termination, which occurred between April and May (Figure
286 3), as defined by the point in time when community losses outweigh the growth rate (Thomalla et al., 2011).



287 **Figure 3: Time series, area-averaged (6 x 1° rectangular sample area, positioned 6° upstream longitudinally, and 1° latitudinally**
 288 **centred around each station) remotely sensed CbPM-PP (mg C m⁻² day⁻¹), monthly average from 08/2016 to 08/2017, dashed vertical**
 289 **lines indicate sampling date.**
 290

291 In deeper waters along the transect, south of the STF, (below 2000 m) where remineralisation is minimal compared to the
 292 mesopelagic zone, our Ba_{xs} concentration of 161 ± 43 pmol L⁻¹ (mean ± SD, n = 15) is not significantly different from the
 293 widely used Ba_{residual} concentration of 180 pmol L⁻¹, measured during early Spring to late Summer (e.g., Jacquet et al., 2008a;
 294 2008b; 2011; 2015; Planchon et al., 2013). We thus did not observe a wintertime decline to an expected “true” SO background
 295 value, when PP and bacterial activity are suspected to be minimal (Jacquet et al., 2011). There are two possible explanations
 296 for this; firstly, the decline to a winter background signal might never be achieved due to ongoing barite precipitation and
 297 remineralisation, as well as the release of labile Ba attached to phytoplankton as they decay, precipitating into barite crystals,
 298 which could possibly continue throughout winter (Cardinal et al., 2005). Secondly, the low sinking speed of suspended barite
 299 (~ 0.3 m d⁻¹, Sternberg et al., 2008), once produced in the mesopelagic layer, implies that it would take ~ 6 years (not
 300 considering reaggregation and redissolution) to sink from 300 m (~ peak of production) to the bottom of the mesopelagic layer
 301 (1000 m depth). The “true” background value may thus have to be measured at the very end of winter just before the initiation
 302 of the spring bloom. This also suggests that the Ba_{xs} signal in the mesopelagic layer may represent remineralisation activity
 303 over more than a few days to weeks, per previous reports (e.g., Dehairs et al., 1997; Jacquet et al., 2015; Planchon et al., 2013).

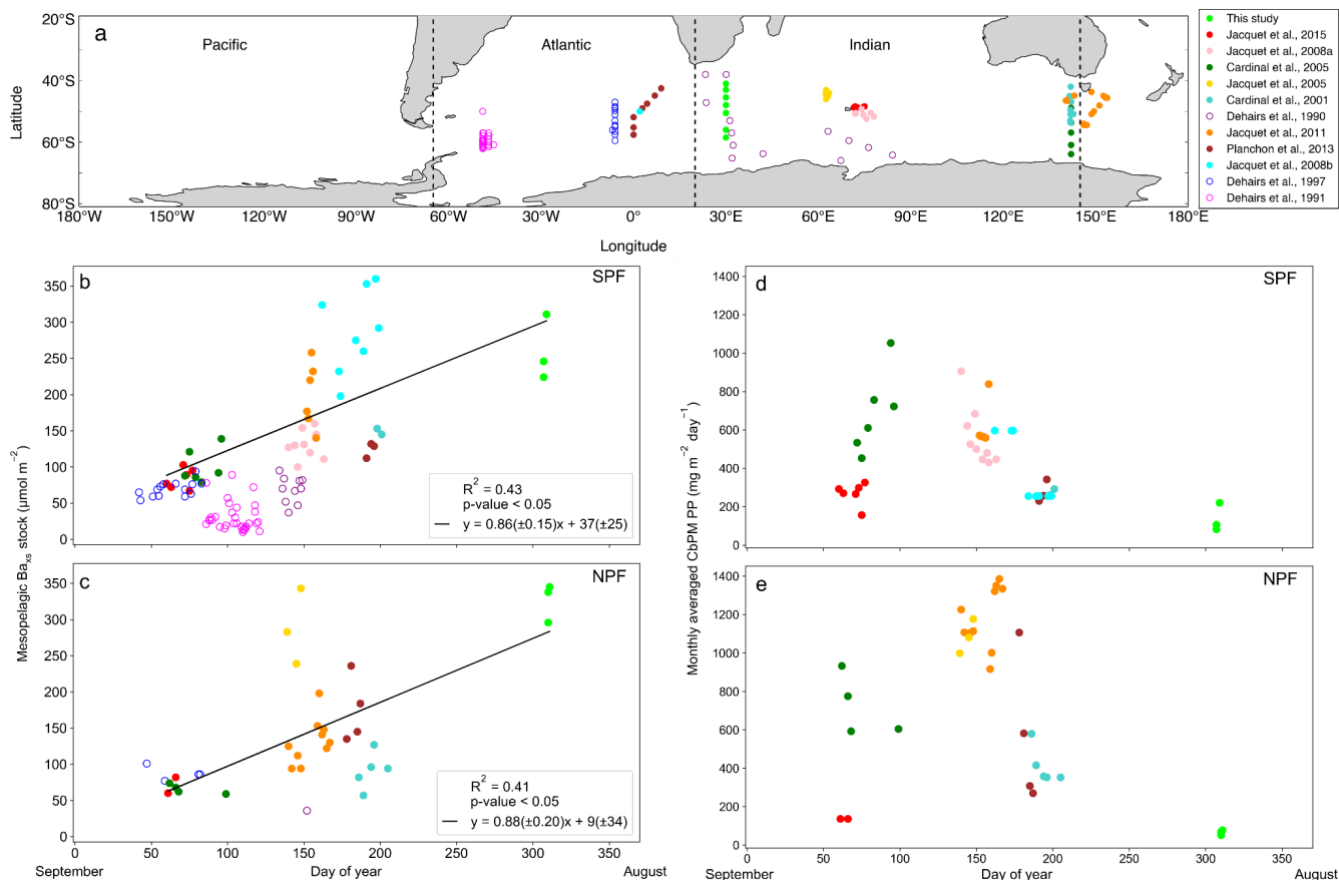
304 4.2 Timescale of the mesopelagic Ba_{xs} signal

305 The Ba_{xs} signal that we observed in winter is in agreement with the suggestion by Dehairs et al. (1997), that there can be
 306 significant carry over between bloom seasons. Other studies have also pointed out that the timescale of this proxy is longer
 307 than a snapshot view (Cardinal et al., 2005) and have highlighted a seasonal increase in mesopelagic Ba_{xs} (Jacquet et al., 2011).
 308 This strongly suggests that the Ba_{xs} signal is not directly linked to synoptic measurements of PP at the time of sampling. In
 309 order to investigate this hypothesis, for the first time, we compiled a SO mesopelagic Ba_{xs} stock dataset with all available

310 literature data including data from this study (Figure 4a, Table S3). The mesopelagic Ba_{xs} stock was integrated over the Ba_{xs}
311 peak depth range (as identified in each study). As can be seen on the map of the compilation dataset (Figure 4a), these data
312 points were collected across the three basins of the SO, over ~ 20 years. Despite this diversity in observations, a statistically
313 significant accumulation of mesopelagic Ba_{xs} with time is still observed, SPF (Figures 4b) and NPF (Figures 4c). Mesopelagic
314 Ba_{xs} accumulates at a rate of $0.86 (\pm 0.15) \mu\text{mol m}^{-2} \text{d}^{-1}$ SPF ($R^2 = 0.43$, p-value < 0.05 , $n = 43$; Figure 4b), and at $0.88 (\pm 0.20)$
315 $\mu\text{mol m}^{-2} \text{d}^{-1}$ NPF ($R^2 = 0.41$, p-value < 0.05 , $n = 31$; Figure 4c), with no statistically significant difference between the two
316 regions (Welch's t-test = 0.24; p-value = 0.80).

317 A possible link between the integrated mesopelagic Ba_{xs} stock and the corresponding integrated remotely sensed PP was
318 assessed for all studies conducted after September 1997, when remotely sensed PP data became available. To do so, we first
319 estimated that sub millimetre sized aggregates would take ~ 20 days to sink down to 1000 m (considered as the bottom of the
320 mesopelagic zone in this study), using a sinking speed of 50 m d^{-1} , that corresponds to an average literature value (50 - 100 m
321 d^{-1} : Riebesell et al., 1991; 50 - 430 m d^{-1} around South Georgia: Cavan et al. 2015; mean of ~ 100 m d^{-1} in the SO as reviewed
322 in Laurenceau-Cornec et al., 2015; Marguerite Bay: 10 - 150 m d^{-1} : McDonnell and Buesseler, 2010). Assuming a maximum
323 surface current speed of 0.2 m s^{-1} (Ferrari and Nikurashin, 2010), it was estimated that these aggregates would have originated,
324 346 km west from the station that was sampled for mesopelagic Ba_{xs} , ~ 20 days prior. Using this distance, the dimensions of
325 the sample area were set with the southernmost station (TM1) of this study, where degrees of longitude cover the smallest
326 area. For the sake of consistency this sample area was applied to all sampling locations of the considered dataset. The integrated
327 remotely sensed PP (see section 2.5) was then averaged spatially, positioned 6° upstream longitudinally, and 1° latitudinally
328 centred around each station, in order to capture the surface PP that is assumed to translate to the mesopelagic remineralisation
329 and measured Ba_{xs} stock.

330 The monthly averaged remotely sensed PP, at the time of sampling, was compiled for the considered dataset, and we found
331 that the PP over the growing season (Figure 4d & e) reaches highest values between January and February (day 125 to 175 of
332 the year), thereafter, steadily decreasing to minimal values in July (~ day 310 of the year, i.e., during our study). The
333 mesopelagic Ba_{xs} accumulation over time can, therefore, not be matched with the remotely sensed PP measured during the
334 month of sampling. A possible relationship between mesopelagic Ba_{xs} stock and temporally integrated remotely sensed PP
335 was further investigated by considering longer timescales. Remotely sensed PP of the preceding bloom was temporally
336 integrated from the preceding September, prior to sampling, as the start of the bloom, in general agreement with previous
337 bloom phenology studies (Thomalla et al., 2011), up to one month prior to the sampling date of the study, taking into
338 consideration time needed for export, aggregate formation and barite crystal release through remineralisation (~ 1 month).

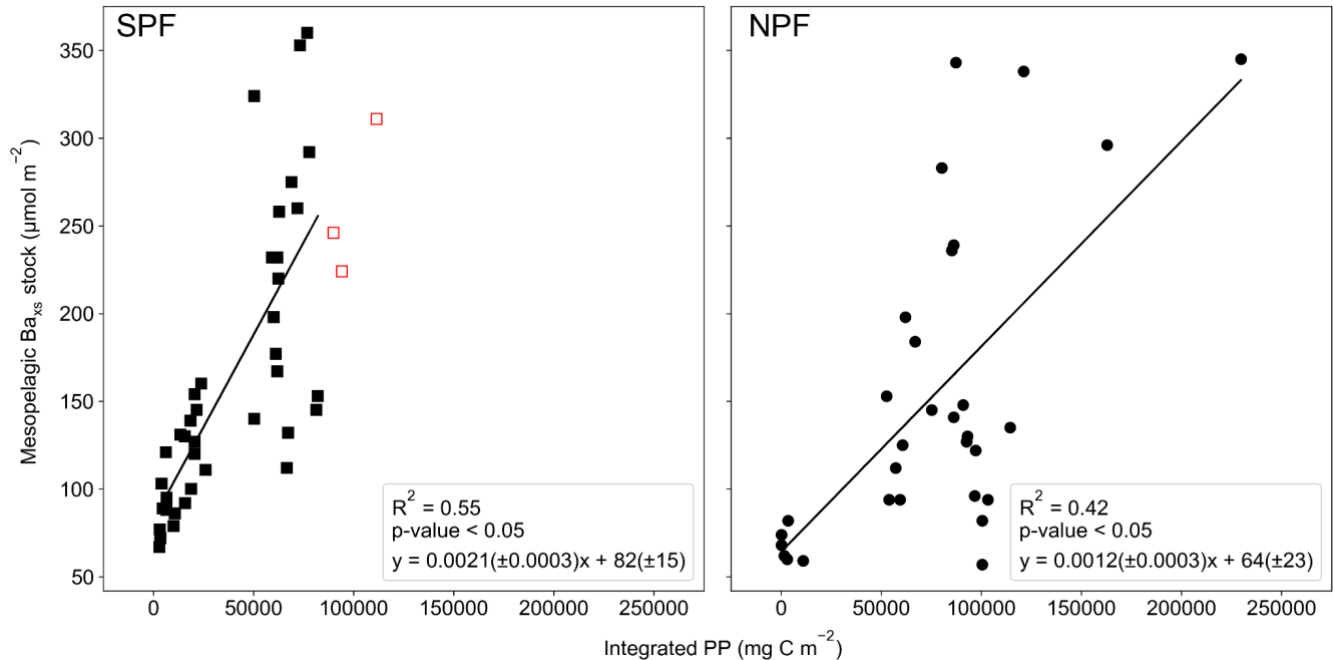


339

340 **Figure 4: (a) Positions of Ba_{xs} observations compiled from all known SO studies, on a cylindrical equal-area projection of the SO, the three SO basin cut offs are indicated by the dashed black lines, from left to right, Pacific, Atlantic and Indian. Integrated mesopelagic Ba_{xs} stock plotted against day of year sampled, with the 1st of September set as day 1, for all available literature data and winter data from this study. Data was split into two zones using the Polar Front (PF) to divide the SO; (b) South of the PF (SPF) and (c) North of the PF (NPF). Monthly averaged remotely sensed PP plotted against day of year, for locations and dates of the SO compilation dataset and winter data from this study; (d) SPF and (e) NPF. Open circles are data points from studies which did not use HF in the particulate sample digestion procedure, regressions did not include these data, there was, however, no significant difference when including these data points (Table S3).**

348 Varying timescales were considered between the preceding September up to 1 month prior to sampling (Sept - T1; Table S4),
 349 in monthly increments, that could influence the relationship between remotely sensed PP and the mesopelagic Ba_{xs} stock (Table
 350 S4). The strongest and most significant correlation between the mesopelagic Ba_{xs} stock and integrated remotely sensed PP, for
 351 both north and south of the PF, was obtained from the preceding September up to 1 month prior to sampling (Table S4, Sept -
 352 T1, SPF: Figure 5a, R² = 0.55, p-value < 0.05, n = 39; NPF: Figure 5b, R² = 0.42, p-value < 0.05, n = 31). When remote sensing
 353 data was limited due to cloud cover and low sunlight during winter months, specifically at the southernmost stations, all
 354 available data was used for the duration of the season. The correlation observed in the STZ is not significant at a 95 %
 355 confidence level (p-value = 0.10); however, the limited number of data points (n = 6) may preclude any significance from

356 emerging. The significant positive correlations obtained south of the STF suggest that mesopelagic Ba_{xs} stock can be used as
 357 a remineralisation proxy on an annual timescale instead of only a few weeks. Figure 5 also reveals that for a given PP the
 358 mesopelagic Ba_{xs} stock was 2-fold higher SPF compared to NPF (Welch's t-test, t-statistic = 2.24; p-value < 0.05), this is
 359 further discussed below.
 360



361
 362 **Figure 5: Integrated mesopelagic Ba_{xs} stock plotted against integrated remotely sensed PP from the preceding September up to one**
 363 **month prior to sampling, all available literature data and winter data from this study, (a) South of the PF (SPF, black squares) and**
 364 **(b) North of the PF (NPF, black circles). Red open squares are data points from our winter dataset where there was not sufficient**
 365 **remote sensing PP data to integrate up to 1 month prior to sampling and available data up to 3 months prior to sampling was plotted**
 366 **but not included in the statistical analysis.**

367 4.3 Environmental factors influencing mesopelagic remineralisation and carbon export efficiency

368 Estimated POC remineralisation fluxes along the transect ($6 - 96 \text{ mg C m}^{-2} \text{ d}^{-1}$) were on the upper end of the range of fluxes
 369 reported in previous studies, with the exception of the STZ station, but within the same order of magnitude for the SO as
 370 estimated from spring to autumn ($0.2 - 118 \text{ mg C m}^{-2} \text{ d}^{-1}$; Table S3; Cardinal et al., 2005; Jacquet et al., 2011, 2015; Planchon
 371 et al., 2013). As the bloom season progresses, more efficient remineralisation rates have been reported in multiple studies
 372 (Cardinal et al., 2005; Jacquet et al., 2011; Planchon et al., 2013). However, during late summer as the bloom declines,
 373 observations indicate an inefficient BCP due to enhanced surface nutrient recycling (Dehairs et al., 1992; Jacquet et al., 2011;
 374 Planchon et al., 2013), leading to a decrease in surface POC export (Planchon et al., 2013). Seasonal variation is reported to
 375 be more pronounced northwards within the SO with the least variation observed in the southern Antarctic circumpolar current
 376 (Dehairs et al., 1997; Planchon et al., 2013).

377 The percentage of mesopelagic POC remineralisation as calculated from estimated POC remineralisation fluxes over integrated
378 remotely sensed PP, for the SO compilation dataset (SPF; 19 ± 15 %, $n = 39$ and NPF; 10 ± 10 %, $n = 29$; mean \pm SD; t-
379 statistic = 2.75; p-value <0.05; Table S3), was ~ 2 fold higher SPF than NPF, revealing the higher surface carbon export
380 efficiency SPF. Our estimates of % POC remineralised fall within the range of reported export efficiencies throughout the SO
381 (2 - 58 %; Jacquet et al., 2011; Morris et al., 2007; Savoye et al., 2008). Our values also support the inverse relationship
382 between export efficiency and productivity, with higher export efficiency in areas of lower production (High Productivity Low
383 E-ratio (HPLE), where E-ratio refers to the ratio between export production and net primary productivity, Fan et al., 2020;
384 Maiti et al., 2013). Estimated mesopelagic POC remineralisation has been reported to account for a significant fraction of
385 exported carbon in the PFZ and southwards, from 31 to 97 %, from spring to summer, whereas it only accounts for ~ 50 % in
386 the SAZ and SAF, during summer (Cardinal et al., 2005). A combination of variables can influence surface export efficiency
387 and the magnitude of the subsequent mesopelagic remineralisation, even more so when considering longer timescales. These
388 variables include physical dynamics and interlinked biogeochemical factors, i.e., bacterial activity, phytoplankton community
389 structure, zooplankton grazing and nutrient availability (Bopp et al., 2013; Buesseler and Boyd, 2009; Cardinal et al., 2005;
390 Jacquet et al., 2008b; Pyle et al., 2018). In previous studies, supply and loss via physical transport has been deemed negligible
391 relative to decay and loss via production, due to minimal advection and diffusion gradients observed on the timescale of days
392 to weeks. These processes were therefore assumed to have minimal impact on the mesopelagic signal (Dehairs et al., 1997;
393 Planchon et al., 2013; Rutgers van der Loeff et al., 2011). It has, however, been observed that features such as mesoscale
394 eddies can have an effect on Ba_{xs} distribution by influencing particle patterns on a broad spatial scale, homogenising
395 mesopelagic remineralisation signals by causing relatively flat profiles or shallower remineralisation peaks (Buesseler et al.,
396 2005; Jacquet et al., 2008b). The region of our winter study is known for being a mesoscale eddy hotspot due to the South-
397 West Indian Ridge (Ansorge et al., 2015). In the STZ, extremely dynamic submesoscale activity due to the Agulhas return
398 current may indeed have significantly influenced the mesopelagic signal, and may help explain the absence of correlation with
399 integrated surface PP. On the contrary, south of the STF, the significant correlations seem to indicate that physical transport
400 variability is not the main process affecting the mesopelagic Ba_{xs} signal, and that biogeochemical factors may be dominant.
401 The Fe-limited SAZ (Ryan-Keogh et al., 2018) and AZ (Viljoen et al., 2018) have generally mixed and seasonally changing
402 assemblages of pico-, nano- and micro-phytoplankton (Eriksen et al., 2018; Gall et al., 2001). Diatoms tend to dominate in the
403 silicate-rich waters south of the PF (Petrou et al., 2016; Rembauville et al., 2017; Wright et al., 2010), whilst seasonally silicate-
404 limited waters north of the PF, favour smaller phytoplankton groups (Freeman et al., 2018; Nissen et al., 2018; Trull et al.,
405 2018). HPLE regimes are indeed characteristic of large areas of the SAZ. They are mainly due to surface POC accumulation
406 caused by non-sinking particles, tending towards less efficient export of smaller cells (Fan et al., 2020). Even when large
407 particles are abundant in HPLE surface layers, a complex grazing community may prevent the export of large particles (Dehairs
408 et al., 1992; Lam and Bishop, 2007). This can explain the higher surface carbon export efficiency that we estimate SPF
409 compared to NPF. Export efficiency has also been linked to bacterial productivity with efficient surface remineralisation
410 limiting surface POC export, when most of the water column integrated bacterial productivity is restricted to the upper mixed

411 layer (Dehairs et al., 1992; Jacquet et al., 2011), which can be the case to varying degrees throughout the SO. In the STZ
412 phytoplankton communities are reported to be dominated by prokaryotic picoplankton including cyanobacteria and
413 prochlorophytes (Mendes et al., 2015). These groups utilise regenerated nutrients in the surface mixed layer tending towards
414 diminished surface export efficiency with high concentrations of non-sinking POC (Fan et al., 2020; Planchon et al. 2013). In
415 addition to this, the potential influence of high submesoscale activity, may explain the low mesopelagic Ba_{xs} measured at the
416 STZ station of this study, despite it being the station with the highest integrated PP (Figure S1). Linking temporally integrated
417 remotely sensed PP to mesopelagic Ba_{xs} stock, coupled with the added influence of physical dynamics affecting surface export
418 efficiencies, along longer timescales, could give better estimates of export and remineralisation signals throughout the SO, on
419 an annual and basin scale. Our estimates of percentage remineralised POC over remotely sensed PP may contribute to the
420 improved modelling of the C cycle over the SO, on an annual timescale.

421 **5 Conclusions**

422 Our unique early winter Ba_{xs} data were similar in magnitude and exhibited the same relationship with σ_θ and dissolved O_2
423 gradients as observed in summer, indicating that processes controlling this signal in summer are still driving the signal in early
424 winter. The expected decline of the mesopelagic Ba_{xs} signal to background values during winter was not observed in this study,
425 supporting the hypothesis that this remineralisation proxy likely has a longer timescale than previously reported. The absolute
426 decline might be delayed due to the cumulative behaviour of mesopelagic Ba_{xs} , ongoing remineralisation and barite
427 precipitation. The “true” SO background value may thus have to be measured at the very end of winter, prior to bloom initiation.
428 Significant positive correlations north and south of the PF, between mesopelagic Ba_{xs} stock and remotely sensed PP, integrated
429 from September to 1 month before sampling (Sept - T1), in combination with significant Ba_{xs} accumulation trends obtained
430 for the SO compilation dataset, suggest an annual timescale. They may also indicate that physical processes do not dominate
431 the mesopelagic signal on an annual scale, within the SO, and that biogeochemical factors are dominant. There is no significant
432 difference in mesopelagic Ba_{xs} and POC remineralisation, north and south of the PF, but the significantly higher integrated
433 remotely sensed PP to the north when compared to the south, indicates a greater export efficiency south of the PF. This is in
434 accordance with the phenomenon of HPLE regimes which are common throughout the SO, moreso north of the PF than south
435 of the PF (Fan et al., 2020). The longer timescale of Ba_{xs} and the cumulative behaviour of this proxy in the mesopelagic zone
436 make it possible to use Ba_{xs} on an annual scale for the estimation of POC remineralisation fluxes throughout the SO and to
437 better understand how variable environmental factors influence these processes on a basin scale. We believe that the
438 significance of these relationships will improve as more data become available (e.g., GEOTRACES IDP2021), which will
439 assist in better understanding and constraining the timescale of remineralisation and C export efficiency throughout the SO.

440 6 Author contribution

441 This study was conceptualised by N.R.vH, H.P, G.S and E.B. Formal analysis, investigation and validation of data was carried
442 out by N.R.vH, H.P, G.S, E.B and T.J.R-K. N.R.vH and T.J.R-K contributed towards the visualisation of the data. H.P, G.S,
443 T.N.M, A.R, N.L. and E.B contributed towards supervision and resources. Funding was acquired by N.R.vH, T.N.M, A.R and
444 E.B. All authors contributed towards writing, reviewing, and editing of the final manuscript.

445 7 Acknowledgments

446 This work was supported by the ISblue project, Interdisciplinary graduate school for the blue planet (ANR-17-EURE-0015)
447 and co-funded by a grant from the French government under the program "Investissements d'Avenir". International
448 collaboration was made possible by funding received by the French-South African National Research Foundation (NRF)
449 Collaboration (PROTEA; FSTR180418322331), NRF funding (SNA170518231343 and UID 110715) including funding from
450 South African Department of Science and Technology, French Ministry of National Education, Higher Education and
451 Research, and the French Ministry of Foreign Affairs and International Development. We would like to thank the captain and
452 crew of the R/V *SA Agulhas II* for their invaluable efforts, as well as all the research participants who assisted our fieldwork.
453 Thanks to Prof. I Ansonge, Dr M du Plessis and Dr E Portela for their assistance with water mass identification, and Dr C.
454 Jeandel for her invaluable expert insight. Finally, we thank the three reviewers, Prof. F. Dehairs, Dr S. Jacquet, and Prof. J.
455 Bishop, for their insightful reviews, thereby improving the quality of our manuscript. A special thank you to Prof. F. Dehairs
456 for sharing the Indigo 3, EPOS 2 and ANTX/6 data.

457 8 References

- 458 Anilkumar, N. and Sabu, P.: Physical process influencing the ecosystem of the indian sector of southern ocean-An overview,
459 Proc. Indian Natl. Sci. Acad., 83(2), 363–376, doi:10.16943/ptinsa/2017/48960, 2017.
- 460 Ansonge, I. J., Jackson, J. M., Reid, K., Durgadoo, J. V, Swart, S. and Eberenz, S.: Evidence of a southward eddy corridor in
461 the South-West Indian ocean, Deep. Res. Part II Top. Stud. Oceanogr., 119, 69–76, doi:10.1016/j.dsr2.2014.05.012, 2015.
- 462 Armstrong, R. A., Peterson, M. L., Lee, C. and Wakeham, S. G.: Settling velocity spectra and the ballast ratio hypothesis,
463 Deep. Res. Part II Top. Stud. Oceanogr., 56(18), 1470–1478, doi:10.1016/j.dsr2.2008.11.032, 2009.
- 464 Barbur, V. A., Montgomery, D. C. and Peck, E. A.: Introduction to Linear Regression Analysis., Stat., 43(2), 339,
465 doi:10.2307/2348362, 1994.
- 466 Behrenfeld, M. J., Boss, E., Siegel, D. A. and Shea, D. M.: Carbon-based ocean productivity and phytoplankton physiology
467 from space, Global Biogeochem. Cycles, 19(1), 1–14, doi:10.1029/2004GB002299, 2005.
- 468 Bishop, J. K. B.: The barite-opal-organic carbon association in oceanic particulate matter, Nature, 332(6162), 341–343,
469 doi:10.1038/332341a0, 1988.

- 470 Bishop, J. K. B. and Edmond, J. M.: A new large volume filtration system for the sampling of oceanic particulate matter, *J.*
471 *Mar. Res.*, 34, 181-198, 1976.
- 472 Bopp, L., Resplandy, L., Orr, J. C., Doney, S. C., Dunne, J. P., Gehlen, M., Halloran, P., Heinze, C., Ilyina, T., Séférian, R.,
473 Tjiputra, J. and Vichi, M.: Multiple stressors of ocean ecosystems in the 21st century: Projections with CMIP5 models,
474 *Biogeosciences*, 10(10), 6225–6245, doi:10.5194/bg-10-6225-2013, 2013.
- 475 Boyd, P. W., Claustre, H., Levy, M., Siegel, D. A. and Weber, T.: Multi-faceted particle pumps drive carbon sequestration in
476 the ocean, *Nature*, 568(7752), 327–335, doi:10.1038/s41586-019-1098-2, 2019.
- 477 Broecker, W. S., Takahashi, T. and Takahashi, T.: Sources and flow patterns of deep-ocean waters as deduced from potential
478 temperature, salinity, and initial phosphate concentration, *J. Geophys. Res. Ocean.*, 90(C4), 6925–6939,
479 doi:10.1029/JC090iC04p06925, 1985.
- 480 Buesseler, K. O.: The decoupling of production and particulate export in the surface ocean, *Global Biogeochem. Cycles*, 12(2),
481 297–310, doi:10.1029/97GB03366, 1998.
- 482 Buesseler, K. O., Andrews, J. E., Pike, S. M., Charette, M. A., Goldson, L. E., Brzezinski, M. A. and Lance, V. P.: Particle
483 export during the Southern Ocean Iron Experiment (SOFeX), *Limnol. Oceanogr.*, 50(1), 311–327,
484 doi:10.4319/lo.2005.50.1.0311, 2005.
- 485 Buesseler, K. O. and Boyd, P. W.: Shedding light on processes that control particle export and flux attenuation in the twilight
486 zone of the open ocean, *Limnol. Oceanogr.*, 54(4), 1210–1232, doi:10.4319/lo.2009.54.4.1210, 2009.
- 487 Cardinal, D., Dehairs, F., Cattaldo, T. and André, L.: Geochemistry of suspended particles in the Subantarctic and Polar
488 Frontal zones south of Australia: Constraints on export and advection processes, *J. Geophys. Res. Ocean.*, 106(C12),
489 31637–31656, doi:10.1029/2000JC000251, 2001.
- 490 Cardinal, D., Savoye, N., Trull, T. W., André, L., Kopczynska, E. E. and Dehairs, F.: Variations of carbon remineralisation in
491 the Southern Ocean illustrated by the Baxs proxy, *Deep. Res. Part I Oceanogr. Res. Pap.*, 52(2), 355–370,
492 doi:10.1016/j.dsr.2004.10.002, 2005.
- 493 Cavan, E. L., Le Moigne, F. A. C., Poulton, A. J., Tarling, G. A., Ward, P., Daniels, C. J., Fragoso, G. M. and Sanders, R. J.:
494 Attenuation of particulate organic carbon flux in the Scotia Sea, Southern Ocean, is controlled by zooplankton fecal pellets,
495 *Geophys. Res. Lett.*, 42(3), 821–830, doi:10.1002/2014GL062744, 2015.
- 496 Cutter, G., Casciotti, K., Croot, P., Geibert, W., Heimbürger, L.-E., Lohan, M., Planquette, H. and van de Flierdt, T.: Sampling
497 and Sample-handling Protocols for GEOTRACES Cruises. Version 3, 139pp. & Appendices [online] Available from:
498 <http://www.geotraces.org/images/stories/documents/intercalibration/Cookbook.pdf>, 2017.
- 499 de Boyer Montégut, C., Madec, G., Fischer, A. S., Lazar, A. and Iudicone, D.: Mixed layer depth over the global ocean: An
500 examination of profile data and a profile-based climatology, *J. Geophys. Res. C Ocean.*, 109(12), 1–20,
501 doi:10.1029/2004JC002378, 2004.
- 502 Dehairs, F., Baeyens, W. and Goeyens, L.: Accumulation of Suspended Barite at Mesopelagic Depths and Export Production
503 in the Southern Ocean, *Science (80-.)*, 258(5086), 1332–1335, doi:10.1126/SCIENCE.258.5086.1332, 1992.

504 Dehairs, F., Chesselet, R. and Jedwab, J.: Discrete suspended particles of barite and the barium cycle in the open ocean, *Earth*
505 *Planet. Sci. Lett.*, 49(2), 528–550, doi:10.1016/0012-821X(80)90094-1, 1980.

506 Dehairs, F. and Goeyens, L.: Oxidation rate of organic carbon in the mesopelagic water column as traced by suspended barium-
507 barite, *Integr. Mar. Syst. Anal.*, 205–217, 1996.

508 Dehairs, F., Goeyens, L., Stroobants, N., Bernard, P., Goyet, C., Poisson, A. and Chesselet, R.: On suspended barite and the
509 oxygen minimum in the Southern Ocean, *Global Biogeochem. Cycles*, 4(1), 85–102, doi:10.1029/GB004I001P00085,
510 1990.

511 Dehairs, F., Shopova, D., Ober, S., Veth, C. and Goeyens, L.: Particulate barium stocks and oxygen consumption in the
512 Southern Ocean mesopelagic water column during spring and early summer: Relationship with export production, *Deep.*
513 *Res. Part II Top. Stud. Oceanogr.*, 44(1–2), 497–516, doi:10.1016/S0967-0645(96)00072-0, 1997.

514 Dehairs, F., Stroobants, N. and Goeyens, L.: Suspended barite as a tracer of biological activity in the Southern Ocean, *Mar.*
515 *Chem.*, 35(1–4), 399–410, doi:10.1016/S0304-4203(09)90032-9, 1991.

516 de Jong, E., Vichi, M., Mehlmann, C. B., Eayrs, C., De Kock, W., Moldenhauer, M. and Audh, R. R.: Sea Ice conditions within
517 the Antarctic Marginal Ice Zone in winter 2017, onboard the SA Agulhas II., Univ. Cape Town, PANGAEA,
518 doi:https://doi.org/10.1594/PANGAEA.885211, 2018.

519 DeVries, T. and Weber, T.: The export and fate of organic matter in the ocean: New constraints from combining satellite and
520 oceanographic tracer observations, *Global Biogeochem. Cycles*, 31(3), 535–555, doi:10.1002/2016GB005551, 2017.

521 Ducklow, H. W., Steinberg, D. K. and Buesseler, K. O.: Upper ocean carbon export and the biological pump, *Oceanography*,
522 14(SPL.ISS. 4), 50–58, doi:10.5670/oceanog.2001.06, 2001.

523 Dymond, J., Suess, E. and Lyle, M.: Barium in Deep-Sea Sediment: A Geochemical Proxy for Paleoproductivity,
524 *Paleoceanography*, 7(2), 163–181, doi:10.1029/92PA00181, 1992.

525 Ehrhardt, M. (Manfred), Grasshoff, K., Kremling, K. (Klaus) and Almgren, T., Eds.: *Methods of seawater analysis / edited by*
526 *K. Grasshoff, M. Ehrhardt, K. Kremling; with contributions by T. Almgren ... [et al.], Verlag Chemie, Weinheim., 1983.*

527 Eriksen, R., Trull, T. W., Davies, D., Jansen, P., Davidson, A. T., Westwood, K. and Van Den Eenden, R.: Seasonal succession
528 of phytoplankton community structure from autonomous sampling at the Australian Southern Ocean Time Series (SOTS)
529 observatory, *Mar. Ecol. Prog. Ser.*, 589, 13–21, doi:10.3354/meps12420, 2018.

530 Fan, G., Han, Z., Ma, W., Chen, S., Chai, F., Mazloff, M. R., Pan, J. and Zhang, H.: Southern Ocean carbon export efficiency
531 in relation to temperature and primary productivity, *Sci. Rep.*, 10(1), 1–11, doi:10.1038/s41598-020-70417-z, 2020.

532 Ferrari, R. and Nikurashin, M.: Suppression of eddy diffusivity across jets in the Southern Ocean, *J. Phys. Oceanogr.*, 40(7),
533 1501–1519, doi:10.1175/2010JPO4278.1, 2010.

534 Freeman, N. M., Lovenduski, N. S., Munro, D. R., Krumhardt, K. M., Lindsay, K., Long, M. C. and MacLennan, M.: The
535 Variable and Changing Southern Ocean Silicate Front: Insights from the CESM Large Ensemble, *Global Biogeochem.*
536 *Cycles*, 32(5), 752–768, doi:10.1029/2017GB005816, 2018.

537 Friedlingstein, P., Jones, M. W., O'Sullivan, M., Andrew, R. M., Hauck, J., Peters, G. P., Peters, W., Pongratz, J., Sitch, S.,
538 Le Quéré, C., Bakker, D. C. E., Canadell, J. G., Ciais, P., Jackson, R. B., Anthoni, P., Barbero, L., Bastos, A., Bastrikov,
539 V., Becker, M., Bopp, L., Buitenhuis, E., Chandra, N., Chevallier, F., Chini, L. P., Currie, K. I., Feely, R. A., Gehlen, M.,
540 Gilfillan, D., Gkritzalis, T., Goll, D. S., Gruber, N., Gutekunst, S., Harris, I., Haverd, V., Houghton, R. A., Hurtt, G., Ilyina,
541 T., Jain, A. K., Joetzjer, E., Kaplan, J. O., Kato, E., Klein Goldewijk, K., Korsbakken, J. I., Landschützer, P., Lauvset, S.
542 K., Lefèvre, N., Lenton, A., Lienert, S., Lombardozi, D., Marland, G., McGuire, P. C., Melton, J. R., Metzl, N., Munro,
543 D. R., Nabel, J. E. M. S., Nakaoka, S.-I., Neill, C., Omar, A. M., Ono, T., Peregon, A., Pierrot, D., Poulter, B., Rehder, G.,
544 Resplandy, L., Robertson, E., Rödenbeck, C., Séférian, R., Schwinger, J., Smith, N., Tans, P. P., Tian, H., Tilbrook, B.,
545 Tubiello, F. N., van der Werf, G. R., Wiltshire, A. J. and Zaehle, S.: Global Carbon Budget 2019, *Earth Syst. Sci. Data*,
546 11(4), 1783–1838, doi:10.5194/essd-11-1783-2019, 2019.

547 Gall, M. P., Boyd, P. W., Hall, J., Safi, K. A. and Chang, H.: Phytoplankton processes. Part 1: Community structure during
548 the Southern Ocean Iron Release Experiment (SOIREE), *Deep. Res. Part II Top. Stud. Oceanogr.*, 48(11–12), 2551–2570,
549 doi:10.1016/S0967-0645(01)00008-X, 2001.

550 GEOTRACES Intermediate Data Product Group: The GEOTRACES Intermediate Data Product 2021 (IDP2021), NERC EDS
551 British Oceanographic Data Centre NOC, doi: 10.5285/cf2d9ba9-d51d-3b7c-e053-8486abc0f5fd, 2021.

552 Gill, A. E.: *Atmosphere-ocean dynamics*, NEW YORK, U.S.A., ACADEMIC PRESS INC., 1982.

553 Gregor, L., Lebehot, A. D., Kok, S. and Scheel Monteiro, P. M.: A comparative assessment of the uncertainties of global
554 surface ocean CO₂ estimates using a machine-learning ensemble (CSIR-ML6 version 2019a)-Have we hit the wall?,
555 *Geosci. Model Dev.*, 12(12), 5113–5136, doi:10.5194/gmd-12-5113-2019, 2019.

556 Gruber, N., Landschützer, P. and Lovenduski, N. S.: The variable southern ocean carbon sink, *Ann. Rev. Mar. Sci.*,
557 11(September), 159–186, doi:10.1146/annurev-marine-121916-063407, 2019.

558 Honjo, S., Eglinton, T. I., Taylor, C. D., Ulmer, K. M., Sievert, S. M., Bracher, A., German, C. R., Edgcomb, V., Francois, R.,
559 Deborraiglesias-Rodriguez, M., Van Mooy, B. and Repeta, D. J.: Understanding the role of the biological pump in the global
560 carbon cycle: An imperative for ocean science, *Oceanography*, 27(3), 10–16, doi:10.5670/oceanog.2014.78, 2014.

561 Ito, T., Follows, M. J. and Boyle, E. A.: Is AOU a good measure of respiration in the oceans?, *Geophys. Res. Lett.*, 31(17), 1–
562 4, doi:10.1029/2004GL020900, 2004.

563 Jacquet, S. H. M., Dehairs, F., Cardinal, D., Navez, J. and Delille, B.: Barium distribution across the Southern Ocean frontal
564 system in the Crozet-Kerguelen Basin, *Mar. Chem.*, 95(3–4), 149–162, doi:10.1016/j.marchem.2004.09.002, 2005.

565 Jacquet, S. H. M., Dehairs, F., Dumont, I., Becquevort, S., Cavagna, A. J. and Cardinal, D.: Twilight zone organic carbon
566 remineralization in the Polar Front Zone and Subantarctic Zone south of Tasmania, *Deep. Res. Part II Top. Stud. Oceanogr.*,
567 58(21–22), 2222–2234, doi:10.1016/j.dsr2.2011.05.029, 2011.

568 Jacquet, S. H. M., Dehairs, F., Elskens, M., Savoye, N. and Cardinal, D.: Barium cycling along WOCE SR3 line in the Southern
569 Ocean, *Mar. Chem.*, 106(1-2 SPEC. ISS.), 33–45, doi:10.1016/j.marchem.2006.06.007, 2007.

570 Jacquet, S. H. M., Dehairs, F., Lefèvre, D., Cavagna, A. J., Planchon, F., Christaki, U., Monin, L., André, L., Closset, I. and
571 Cardinal, D.: Early spring mesopelagic carbon remineralization and transfer efficiency in the naturally iron-fertilized
572 Kerguelen area, *Biogeosciences*, 12(6), 1713–1731, doi:10.5194/bg-12-1713-2015, 2015.

573 Jacquet, S. H. M., Dehairs, F., Savoye, N., Obernosterer, I., Christaki, U., Monnin, C. and Cardinal, D.: Mesopelagic organic
574 carbon remineralization in the Kerguelen Plateau region tracked by biogenic particulate Ba, *Deep. Res. Part II Top. Stud.*
575 *Oceanogr.*, 55(5–7), 868–879, doi:10.1016/j.dsr2.2007.12.038, 2008a.

576 Jacquet, S. H. M., Savoye, N., Dehairs, F., Strass, V. H. and Cardinal, D.: Mesopelagic carbon remineralization during the
577 European Iron Fertilization Experiment, *Global Biogeochem. Cycles*, 22(1), 1–9, doi:10.1029/2006GB002902, 2008b.

578 Jochum, K. P., Nohl, U., Herwig, K., Lammel, E., Stoll, B. and Hofmann, A. W.: GeoReM: A new geochemical database for
579 reference materials and isotopic standards, *Geostand. Geoanalytical Res.*, 29(3), 333–338, doi:10.1111/j.1751-
580 908x.2005.tb00904.x, 2005.

581 Kokoska, S. and Zwillinger, D.: CRC Standard Probability and Statistics Tables and Formulae, Student Edition., 2000.

582 Lam, P. J. and Bishop, J. K. B.: High biomass, low export regimes in the Southern Ocean, *Deep. Res. Part II Top. Stud.*
583 *Oceanogr.*, 54(5–7), 601–638, doi:10.1016/j.dsr2.2007.01.013, 2007.

584 Laurenceau-Cornec, E. C., Trull, T. W., Davies, D. M., Bray, S. G., Doran, J., Planchon, F., Carlotti, F., Jouandet, M. P.,
585 Cavagna, A. J., Waite, A. M. and Blain, S.: The relative importance of phytoplankton aggregates and zooplankton fecal
586 pellets to carbon export: Insights from free-drifting sediment trap deployments in naturally iron-fertilised waters near the
587 Kerguelen Plateau, *Biogeosciences*, 12(4), 1007–1027, doi:10.5194/BG-12-1007-2015, 2015.

588 Le Moigne, F. A. C.: Pathways of Organic Carbon Downward Transport by the Oceanic Biological Carbon Pump, *Front. Mar.*
589 *Sci.*, 6, doi:10.3389/fmars.2019.00634, 2019.

590 Legeleux, F. and Reyss, J. L.: $^{228}\text{Ra}/^{226}\text{Ra}$ activity ratio in oceanic settling particles: Implications regarding the use of barium
591 as a proxy for paleoproductivity reconstruction, *Deep. Res. Part I Oceanogr. Res. Pap.*, 43(11–12), 1857–1863,
592 doi:10.1016/S0967-0637(96)00086-6, 1996.

593 Lemaitre, N., Planquette, H., Planchon, F., Sarthou, G., Jacquet, S., García-Ibáñez, M. I., Gourain, A., Cheize, M., Monin, L.,
594 André, L., Laha, P., Terryn, H. and Dehairs, F.: Particulate barium tracing of significant mesopelagic carbon
595 remineralisation in the North Atlantic, *Biogeosciences*, 15(8), 2289–2307, doi:10.5194/bg-15-2289-2018, 2018.

596 Maiti, K., Charette, M. A., Buesseler, K. O. and Kahru, M.: An inverse relationship between production and export efficiency
597 in the Southern Ocean, *Geophys. Res. Lett.*, 40(8), 1557–1561, doi:10.1002/GRL.50219, 2013.

598 Marsay, C. M., Sanders, R. J., Henson, S. A., Pabortsava, K., Achterberg, E. P. and Lampitt, R. S.: Attenuation of sinking
599 particulate organic carbon flux through the mesopelagic ocean, *Proc. Natl. Acad. Sci. U. S. A.*, 112(4), 1089–1094,
600 doi:10.1073/pnas.1415311112, 2015.

601 McDonnell, A. M. P. and Buesseler, K. O.: Variability in the average sinking velocity of marine particles, *Limnol. Oceanogr.*,
602 55(5), 2085–2096, doi:10.4319/LO.2010.55.5.2085, 2010.

- 603 Mendes, C. R. B., Kerr, R., Tavano, V. M., Cavalheiro, F. A., Garcia, C. A. E., Gauns Dessai, D. R. and Anilkumar, N.: Cross-
604 front phytoplankton pigments and chemotaxonomic groups in the Indian sector of the Southern Ocean, *Deep. Res. Part II*
605 *Top. Stud. Oceanogr.*, 118, 221–232, doi:10.1016/j.dsr2.2015.01.003, 2015.
- 606 Morris, P. J., Sanders, R., Turnewitsch, R. and Thomalla, S.: 234Th-derived particulate organic carbon export from an island-
607 induced phytoplankton bloom in the Southern Ocean, *Deep Sea Res. Part II Top. Stud. Oceanogr.*, 54(18–20), 2208–2232,
608 doi:10.1016/J.DSR2.2007.06.002, 2007.
- 609 Nissen, C., Vogt, M., Münnich, M., Gruber, N. and Haumann, F. A.: Factors controlling coccolithophore biogeography in the
610 Southern Ocean, *Biogeosciences*, 15(22), 6997–7024, doi:10.5194/bg-15-6997-2018, 2018.
- 611 Orsi, A. H., Whitworth, T. and Nowlin, W. D.: On the meridional extent and fronts of the Antarctic Circumpolar Current,
612 *Deep. Res. Part I*, 42(5), 641–673, doi:10.1016/0967-0637(95)00021-W, 1995.
- 613 Passow, U. and Carlson, C. A.: The biological pump in a high CO₂ world, *Mar. Ecol. Prog. Ser.*, 470(2), 249–271,
614 doi:10.3354/meps09985, 2012.
- 615 Petrou, K., Kranz, S. A., Trimborn, S., Hassler, C. S., Ameijeiras, S. B., Sackett, O., Ralph, P. J. and Davidson, A. T.: Southern
616 Ocean phytoplankton physiology in a changing climate, *J. Plant Physiol.*, 203, 135–150,
617 doi:https://doi.org/10.1016/j.jplph.2016.05.004, 2016.
- 618 Planchon, F., Cavagna, A. J., Cardinal, D., André, L. and Dehairs, F.: Late summer particulate organic carbon export and
619 twilight zone remineralisation in the Atlantic sector of the Southern Ocean, *Biogeosciences*, 10(2), 803–820,
620 doi:10.5194/bg-10-803-2013, 2013.
- 621 Planquette, H. and Sherrell, R. M.: Sampling for particulate trace element determination using water sampling bottles:
622 Methodology and comparison to in situ pumps, *Limnol. Oceanogr. Methods*, 10(5), 367–388,
623 doi:10.4319/lom.2012.10.367, 2012.
- 624 Pollard, R. T., Lucas, M. I. and Read, J. F.: Physical controls on biogeochemical zonation in the Southern Ocean, *Deep. Res.*
625 *Part II Top. Stud. Oceanogr.*, 49(16), 3289–3305, doi:10.1016/S0967-0645(02)00084-X, 2002.
- 626 Pyle, K. M., Hendry, K. R., Sherrell, R. M., Legge, O., Hind, A. J., Bakker, D., Venables, H. and Meredith, M. P.: Oceanic
627 fronts control the distribution of dissolved barium in the Southern Ocean, *Mar. Chem.*, 204(July), 95–106,
628 doi:10.1016/j.marchem.2018.07.002, 2018.
- 629 Rembauville, M., Briggs, N., Ardyna, M., Uitz, J., Catala, P., Penkerch, C., Poteau, A., Claustre, H. and Blain, S.: Plankton
630 Assemblage Estimated with BGC-Argo Floats in the Southern Ocean: Implications for Seasonal Successions and Particle
631 Export, *J. Geophys. Res. Ocean.*, 122(10), 8278–8292, doi:10.1002/2017JC013067, 2017.
- 632 Riebesell, U.: Particle aggregation during a diatom bloom. II. Biological aspects, *Mar. Ecol. Prog. Ser.*, 69(3), 281–291,
633 doi:10.3354/meps069281, 1991.
- 634 Rio, M. H., Guinehut, S. and Larnicol, G.: New CNES-CLS09 global mean dynamic topography computed from the
635 combination of GRACE data, altimetry, and in situ measurements, *J. Geophys. Res. Ocean.*, 116(7), 1–25,
636 doi:10.1029/2010JC006505, 2011.

637 Robinson, C., Steinberg, D. K., Anderson, T. R., Arístegui, J., Carlson, C. A., Frost, J. R., Ghiglione, J. F., Hernández-León,
638 S., Jackson, G. A., Koppelman, R., Quéguiner, B., Ragueneau, O., Rassoulzadegan, F., Robison, B. H., Tamburini, C.,
639 Tanaka, T., Wishner, K. F. and Zhang, J.: Mesopelagic zone ecology and biogeochemistry - A synthesis, *Deep. Res. Part*
640 *II Top. Stud. Oceanogr.*, 57(16), 1504–1518, doi:10.1016/j.dsr2.2010.02.018, 2010.

641 Rosengard, S. Z., Lam, P. J., Balch, W. M., Auro, M. E., Pike, S., Drapeau, D. and Bowler, B.: Carbon export and transfer to
642 depth across the Southern Ocean Great Calcite Belt, *Biogeosciences*, 12(13), 3953–3971, doi:10.5194/bg-12-3953-2015,
643 2015.

644 Rutgers van der Loeff Michiel, M., Cai, P. H., Stimac, I., Bracher, A., Middag, R., Klunder, M. B. and van Heuven, S. M. A.
645 C.: ²³⁴Th in surface waters: Distribution of particle export flux across the Antarctic Circumpolar Current and in the
646 Weddell Sea during the GEOTRACES expedition ZERO and DRAKE, *Deep. Res. Part II Top. Stud. Oceanogr.*, 58(25–
647 26), 2749–2766, doi:10.1016/j.dsr2.2011.02.004, 2011.

648 Ryan-Keogh, T. J., Thomalla, S. J., Mtshali, T. N., Van Horsten, N. R. and Little, H. J.: Seasonal development of iron limitation
649 in the sub-Antarctic zone, *Biogeosciences*, 15(14), 4647–4660, doi:10.5194/bg-15-4647-2018, 2018.

650 Sarmiento, J., & Gruber, N. *Ocean Biogeochemical Dynamics*, Princeton University Press, Princeton, Oxford
651 doi:10.2307/j.ctt3fgxqx, 2006.

652 Sathyendranath, S., Brewin, R. J. W., Brockmann, C., Brotas, V., Calton, B., Chuprin, A., Cipollini, P., Couto, A. B., Dingle,
653 J., Doerffer, R., Donlon, C., Dowell, M., Farman, A., Grant, M., Groom, S., Horseman, A., Jackson, T., Krasemann, H.,
654 Lavender, S., Martinez-Vicente, V., Mazeran, C., Mélin, F., Moore, T. S., Müller, D., Regner, P., Roy, S., Steele, C. J.,
655 Steinmetz, F., Swinton, J., Taberner, M., Thompson, A., Valente, A., Zühlke, M., Brando, V. E., Feng, H., Feldman, G.,
656 Franz, B. A., Frouin, R., Gould, R. W., Hooker, S. B., Kahru, M., Kratzer, S., Mitchell, B. G., Muller-Karger, F. E., Sosik,
657 H. M., Voss, K. J., Werdell, J. and Platt, T.: An ocean-colour time series for use in climate studies: The experience of the
658 ocean-colour climate change initiative (OC-CCI), *Sensors (Switzerland)*, 19(19), doi:10.3390/s19194285, 2019.

659 Savoye, N., Trull, T. W., Jacquet, S. H. M., Navez, J. and Dehairs, F.: ²³⁴Th-based export fluxes during a natural iron
660 fertilization experiment in the Southern Ocean (KEOPS), *Deep Sea Res. Part II Top. Stud. Oceanogr.*, 55(5–7), 841–855,
661 doi:10.1016/J.DSR2.2007.12.036, 2008.

662 Schlitzer, R.: Carbon export fluxes in the Southern Ocean: Results from inverse modeling and comparison with satellite-based
663 estimates, *Deep. Res. Part II Top. Stud. Oceanogr.*, 49(9–10), 1623–1644, doi:10.1016/S0967-0645(02)00004-8, 2002.

664 Shopova, D., Dehairs, F. and Baeyens, W.: A simple model of biogeochemical element distribution in the oceanic water
665 column, *J. Mar. Syst.*, 6(4), 331–344, doi:10.1016/0924-7963(94)00032-7, 1995.

666 Sigman, D. M., Hain, M. P. and Haug, G. H.: The polar ocean and glacial cycles in atmospheric CO₂ concentration, *Nature*,
667 466(7302), 47–55, doi:10.1038/nature09149, 2010.

668 Sternberg, E., Jeandel, C., Robin, E. and Souhaut, M.: Seasonal cycle of suspended barite in the mediterranean sea, *Geochim.*
669 *Cosmochim. Acta*, 72(16), 4020–4034, doi:10.1016/J.GCA.2008.05.043, 2008.

670 Sternberg, E., Tang, D., Ho, T. Y., Jeandel, C. and Morel, F. M. M.: Barium uptake and adsorption in diatoms, *Geochim.*
671 *Cosmochim. Acta*, 69(11), 2745–2752, doi:10.1016/j.gca.2004.11.026, 2005.

672 Swart, S., Speich, S., Ansorge, I. J. and Lutjeharms, J. R. E.: An altimetry-based gravest empirical mode south of Africa: 1.
673 Development and validation, *J. Geophys. Res. Ocean.*, 115(3), 1–19, doi:10.1029/2009JC005299, 2010.

674 Takahashi, T., Sweeney, C., Hales, B., Chipman, D. W., Goddard, J. G., Newberger, T., Iannuzzi, R. A. and Sutherland, S. C.:
675 The changing carbon cycle in the southern ocean, *Oceanography*, 25(3), 26–37, doi:10.5670/oceanog.2012.71, 2012.

676 Taylor, S. R. and McLennan, S. M.: *The continental crust: Its composition and evolution*, Blackwell Scientific Pub., Palo Alto,
677 CA, United States. [online] Available from: <https://www.osti.gov/biblio/6582885>, 1985.

678 Thomalla, S. J., Fauchereau, N., Swart, S. and Monteiro, P. M. S.: Regional scale characteristics of the seasonal cycle of
679 chlorophyll in the Southern Ocean, *Biogeosciences*, 8(10), 2849–2866, doi:10.5194/bg-8-2849-2011, 2011.

680 Trull, T. W., Passmore, A., Davies, D. M., Smit, T., Berry, K. and Tilbrook, B.: Distribution of planktonic biogenic carbonate
681 organisms in the Southern Ocean south of Australia: A baseline for ocean acidification impact assessment, *Biogeosciences*,
682 15(1), 31–49, doi:10.5194/bg-15-31-2018, 2018.

683 Twining, B. S., Nodder, S. D., King, A. L., Hutchins, D. A., LeClerc, G. R., DeBruyn, J. M., Maas, E. W., Vogt, S., Wilhelm,
684 S. W. and Boyd, P. W.: Differential remineralization of major and trace elements in sinking diatoms, *Limnol. Oceanogr.*,
685 59(3), 689–704, doi:<https://doi.org/10.4319/lo.2014.59.3.0689>, 2014.

686 van Beek, P., François, R., Conte, M., Reyss, J. L., Souhaut, M. and Charette, M.: 228Ra/226Ra and 226Ra/Ba ratios to track
687 barite formation and transport in the water column, *Geochim. Cosmochim. Acta*, 71(1), 71–86,
688 doi:10.1016/j.gca.2006.07.041, 2007.

689 Viljoen, J. J., Philibert, R., Van Horsten, N., Mtshali, T., Roychoudhury, A. N., Thomalla, S. and Fietz, S.: Phytoplankton
690 response in growth, photophysiology and community structure to iron and light in the Polar Frontal Zone and Antarctic
691 waters, *Deep. Res. Part I Oceanogr. Res. Pap.*, 141(September), 118–129, doi:10.1016/j.dsr.2018.09.006, 2018.

692 Wright, S. W., van den Enden, R. L., Pearce, I., Davidson, A. T., Scott, F. J. and Westwood, K. J.: Phytoplankton community
693 structure and stocks in the Southern Ocean (30–80°E) determined by CHEMTAX analysis of HPLC pigment signatures,
694 *Deep. Res. Part II Top. Stud. Oceanogr.*, 57(9–10), 758–778, doi:10.1016/j.dsr2.2009.06.015, 2010.

695 Zhuang, J.: xESMF: Universal Regridder for GeospatialData, <https://github.com/JiaweiZhuang/xESMF>, 2018.

696